CrossMark

The roles of the spatial regularization in seismic deconvolution

**Nan Tian · Tingen Fan · Guangyi Hu · Ruwei Zhang · Jiannan Zhou ·
Jing Le**

Abstract   In this paper we investigate the roles of the spatial regularization in seismic deconvolution. The spatial regularization is described as a L2 norm of the lateral reflectivity difference imposed on multi-trace data misfit term. In essence, the spatial regularization acts as a band-pass filter along the spatial direction. Therefore, it can suppress the high-wavenumber components of the estimated reflectivity, for example, noisy trails like noodles which usually caused by temporal regularized deconvolution. As well, the spatial regularization can help recovering the reflectivity of discarding traces by repeatedly and linearly weighting its neighboring reflectivity, thereby exploring the spatial continuities among traces. Moreover, the spatial regularization can help stabilizing inversion, just like the temporal regularization. Both synthetic and field data examples are used to demonstrate the three roles of the spatial regularization by comparing spatial regularized deconvolution with conventional temporal deconvolution implemented by minimizing a data misfit and a L2 norm or a L1 norm of reflectivity. Furthermore, the synthetic examples also clearly illustrate that the spatial regularization can help yielding a high resolution and meanwhile high signal-to-noise ratio deconvolution result, which matches best with the reference reflectivity.

Keywords   Spatial regularization · Deconvolution · Seismic resolution · Structures

1 Introduction

Generally, the post-stack seismic signal can be assumed as the convolution of seismic wavelet and reflectivity. Since the wavelet is always band-limited, the seismic signal is

---

N. Tian (✉) · T. Fan · G. Hu · J. Zhou · J. Le
CNOOC Research Institute, Taiyanggongnanjie #6, Chaoyang District, Beijing 100028, China
e-mail: tiannan2@cnooc.com.cn

R. Zhang
Guangzhou Marine Geological Survey, Guangzhou 510760, China

band-limited and some important geology details are lost. Therefore, seismic deconvolution to remove the wavelet effect from seismic data is an important step in seismic data processing (e.g. Robinson 1984; Yuan and Wang 2011). However, because of the band-limitation of wavelet and noise, the seismic deconvolution is commonly an ill-posed inverse problem. Many deconvolution and reflectivity inversion methods (e.g. Taylor et al. 1979; Levy and Fullagar 1981; Debeye and van Riel 1990; Sacchi 1997; Herrmann 2005; Baziw and Ulrych 2006; Wu et al. 2007; Yuan and Wang 2013a) had been introduced to address the issue by adding a regularization or a constraint along the temporal direction and successfully applied on various seismic data sets and have the advantages that they are very fast and favor parallel computation. However, these techniques are realized trace by trace. Besides ignoring the spatial connection among traces, trace-by-trace processing often suffer from the lateral instability of the estimated reflectivity or impedance (e.g. Zhang et al. 2013; Yuan et al. 2015), probably mainly due to the influence of high-wavenumber components in model error or the inconsistency of the energy and waveforms among seismic traces.

Several multi-trace deconvolution or reflectivity inversion methods had been proposed to explore spatial dependencies among traces. For example, Lavielle (1991) proposed a multi-trace non-blind deconvolution method, which makes use of Gibbs distributions and Markov random fields to integrate a priori information to model the lateral coherency of the reflectors. For this multi-trace reflectivity inverse problem, the simulated annealing algorithm is used to locate the global minimum multi-trace reflectivity with a high degree of accuracy. Kaaresen and Taxt (1998) proposed a multi-trace blind deconvolution method to simultaneously invert for a short wavelet with known duration and multi-trace reflectivity with local continuities among neighboring traces by alternatively implementing a least-square algorithm and an iterated window maximization algorithm. Wang et al. (2006) proposed a structure-preserving multi-trace deconvolution method by using adaptive FX filtering to enhance the coherence of seismic events across midpoints. Heimer and Cohen (2008) introduced a multi-trace deconvolution method by using a Markov-Bernoulli random-field modeling combined with the Viterbi algorithm to further explore layer discontinuities. Kumar (2009) proposed a multi-trace non-spiky deconvolution method by using multiscale and multidirectional curvelet transform to exploit the continuities along reflectors for cases in which the assumption of spiky reflectivity may not hold. Zhang et al. (2013) extended the single-trace Basis pursuit reflectivity inversion (2011) to a multi-trace case by adopting a 'Z' shape spatial derivative as a regularization term. Gholami and Sacchi (2013) proposed a fast 3D blind seismic deconvolution method to simultaneously invert for a wavelet with sparseness in a wavelet transform domain and 3D reflectivity along 3D singularities in the time–space domain via a split Bregman iteration algorithm. These works mainly focus on developing different (fast) deconvolution or reflectivity inversion methods with a spatial regularization or a constraint about spatial connection among traces to process 2D or 3D stationary data.

In this paper, we also explore spatial (local) continuities of the reflectivity by adopting a spatial regularization. Furthermore, we focus on clarifying the physical roles of the spatial regularization. Besides preserving spatial continuities of structures, we also believe that the spatial regularization can help stabilizing reflectivity inversion, preventing trails like noodles, and recovering the reflectivity of the missing traces, as explained by the theory and verified by the synthetic and field data examples. In fact, the recovery of the reflectivity for the missing traces implicitly reveals that the spatial regularization can evidently and truly explore lateral continuity of the estimated reflectivity. Moreover, the spatial regularization has an ability to help yielding a high resolution and meanwhile high fidelity

reflectivity result, or achieving a good tradeoff between reflectivity fidelity and resolution improvement, which is obviously observed in our synthetic data example.

2 Theory

According to Robinson and Treitel (1980), a single trace signal in the post-stack seismic data set is widely considered as the convolution of a seismic wavelet with a reflectivity series and can be mathematically written in a matrix–vector form as

$$\mathbf{S}_j = \mathbf{WR}_j, \tag{1}$$

where column vectors $\mathbf{S}_j$ and $\mathbf{R}_j$ represent the j-th trace seismic signal and reflectivity series respectively, the wavelet convolution matrix $\mathbf{W} = \begin{bmatrix} w_1 & 0 & \cdots & 0 \\ w_2 & w_1 & \ddots & \vdots \\ \vdots & w_2 & \ddots & 0 \\ w_L & \vdots & \ddots & w_1 \\ 0 & w_L & \ddots & w_2 \\ \vdots & \ddots & \ddots & \vdots \\ 0 & \cdots & 0 & w_L \end{bmatrix}$ is a Toeplitz

matrix, vector $\mathbf{w} = [w_1, w_2, \ldots, w_L]$ denotes the seismic wavelet and L is the length of the wavelet.

Based on the assumption that the wavelet is spatiotemporal stationary, the multi-trace seismic reflection signal can be described as the following matrix–matrix system according to Eq. (1)

$$\mathbf{S} = \mathbf{WR}, \tag{2}$$

where matrices $\mathbf{S} = [\mathbf{S}_1, \mathbf{S}_2, \ldots, \mathbf{S}_M]$ and $\mathbf{R} = [\mathbf{R}_1, \mathbf{R}_2, \ldots, \mathbf{R}_M]$ with M the number of traces.

Mathematically, Eq. (2) also can be rewritten in a matrix–vector system as follows

$$\mathbf{d} = \mathbf{Gm}, \tag{3}$$

where vector $\mathbf{d} = vec(\mathbf{S})$, matrix $\mathbf{G} = kron(\mathbf{I}, \mathbf{W})$, $\mathbf{I}$ is the identity matrix, vector $\mathbf{m} = vec(\mathbf{R})$, vec means arranging the columns of a matrix into a long concatenated vector, and $kron$ defines a Kronecker product that reformulates matrix–matrix multiplication into matrix–vector product. Note $\mathbf{G}$ is a blocky diagonal matrix and exceedingly sparse with most entries zero.

Assuming that the wavelet $\mathbf{w}$ is known, the multi-trace reflectivity series can be simultaneously estimated by minimizing the following objective function

$$O_1(\hat{\mathbf{m}}) = ||\mathbf{d}^{obs} - \mathbf{Gm}||_2^2, \tag{4}$$

where column vector $\hat{\mathbf{m}} = \left[\hat{\mathbf{R}}_1, \hat{\mathbf{R}}_2, \cdots, \hat{\mathbf{R}}_M \right]^T$, and $\hat{\mathbf{R}}_j$ represents the j-th trace estimated reflectivity. From the viewpoint of inversion, $\mathbf{d}^{obs} = vec(\mathbf{D}^{obs})$ and $\mathbf{Gm}$ represent the observed multi-trace data and the calculated multi-trace data respectively, where $\mathbf{D}^{obs} = [\mathbf{D}_1^{obs}, \mathbf{D}_2^{obs}, \ldots, \mathbf{D}_M^{obs}]$ and $\mathbf{D}_j^{obs}$ represents the j-th trace observed data. Because the length of the seismic wavelet is always limited, the above objective function is a strict convex function at the absence of noise. Therefore, Eq. (4) has a unique minimum

extreme, which can be obtained by taking the derivatives of $O_1(\hat{\mathbf{m}})$ with respect to variables $\mathbf{m}$ to be $\mathbf{0}$. Then a normal equation can be derived as follows

$$\mathbf{G}^T\mathbf{G}\mathbf{m} = \mathbf{G}^T\mathbf{d}^{obs}, \tag{5}$$

where $\mathbf{G}^T\mathbf{G} = kron(\mathbf{I},\mathbf{W}^T\mathbf{W})$ is a non-negative definite square symmetric matrix, and superscript T represents the transpose.

If we perform singular value decomposition (SVD) for matrix $\mathbf{W}$, the solution of Eq. (5) can be given as

$$\hat{\mathbf{m}} = kron\left(\mathbf{I}, \sum_{k=1}^{K} \frac{1}{\delta_k}\mathbf{V}_k\mathbf{U}_k^T\right)\mathbf{d}^{obs}, \tag{6}$$

where $\delta_1 \geq \delta_2 \geq \cdots \geq \delta_K \geq 0$ are singular values of $\mathbf{W}$, column vector $\mathbf{U}_k$ ($k = 1,\ldots,K$) is the left singular vector, and column vector $\mathbf{V}_k$ ($k = 1,2,\ldots,K$) is the right singular vector. Equation (6) means that $\hat{\mathbf{R}}_j$ can be considered as the linear weighted superposition of K eigen-signals $\mathbf{V}_k\mathbf{U}_k^T\mathbf{D}_j^{obs}$ ($k = 1,2,\ldots,K$) with weights $1/\delta_k$. Further, $\hat{\mathbf{R}}_j$ can be regarded as the linear weighted superposition of the K right singular vectors $\mathbf{V}_k$ ($k = 1,\ldots,K$) with weights $\mathbf{U}_k^T\mathbf{D}_j^{obs}/\delta_k$. Since the amplitude of high-frequency components of seismic wavelet is always very small even close to zero mainly due to the absorption of media, matrix $\mathbf{W}$ has many small singular values. In general, the left singular vector $\mathbf{U}_k$ and the right singular vector $\mathbf{V}_k$ corresponding to small singular values commonly act as high-frequency signals, whereas those associated with large singular values own plentiful low-frequency components but very little high-frequency components. When $\mathbf{D}_j^{obs}$ does not include high-frequency noise (or model error) outside the frequency band of wavelet, the dependency of the left singular vector $\mathbf{U}_k$ corresponding to small singular values on $\mathbf{D}_j^{obs}$ ($j = 1,2,\ldots,M$) is poor. Therefore, $\mathbf{U}_k^T\mathbf{D}_j^{obs}/\delta_k$ will not be too large to cause the estimated $\hat{\mathbf{R}}_j$ strongly oscillating. In this case, the reflectivity inversion is stable. However, when $\mathbf{D}_j^{obs}$ includes high-frequency noise (or model error), $\mathbf{U}_k^T\mathbf{D}_j^{obs}/\delta_k$ corresponding to most small singular values will be probably large, thus bringing in strong high-frequency components, further blurring the other frequency components of the estimated $\hat{\mathbf{R}}_j$. In a word, it will give rise to the instability of the inversion.

In this paper, we impose a spatial regularization (Yuan et al. 2012) on Eq. (4) to reduce even overcome this issue. The improved objective function can be given as

$$O_2(\hat{\mathbf{m}}) = ||\mathbf{d}^{obs} - \mathbf{G}\mathbf{m}||_2^2 + \sum_l \gamma_l||\mathbf{C}_l\mathbf{m}||_2^2, \tag{7}$$

where $\mathbf{C}_l$ is a first-order difference operator, which can be taken as the spatial difference along the interpreted horizon(s), dipping spatial direction(s) and/or horizontal spatial direction, and γ_l is regularization parameter(s) determining the balance between the data residual and the smoothness degree or length of $\mathbf{C}_l\mathbf{m}$. We do not take $\mathbf{C}_l$ as a conventional frequency-wavenumber (FK) operator or a scale-position-angle (Curvelet) operator, since minimizing the energy of FK-domain or Curvelet-domain coefficients does not realize the spatial regularization role. Here, we only consider $\mathbf{C}_l$ to be a first-order difference operator along the horizontal direction in order to conveniently clarify the roles of the spatial regularization. Therefore, Eq. (7) can be simplified as

$$O_3(\hat{\mathbf{m}}) = ||\mathbf{d}^{obs} - \mathbf{Gm}||_2^2 + \gamma ||\mathbf{Cm}||_2^2. \tag{8}$$

The function is a typical convex function, since both the data misfit term and the regularization term are convex. The optimum solution of Eq. (8) can be obtained by taking the derivatives of $O_3(\hat{\mathbf{m}})$ with respect to variables $\mathbf{m}$ being $\mathbf{0}$, hence we get

$$\hat{\mathbf{m}} = \left(\mathbf{G}^T\mathbf{G} + \gamma\mathbf{C}^T\mathbf{C}\right)^{-1}\mathbf{G}^T\mathbf{d}^{obs} = \left(\mathbf{G}^T\mathbf{G} + 2\gamma\mathbf{I} + \gamma\mathbf{A}\right)^{-1}\mathbf{G}^T\mathbf{d}^{obs}, \tag{9}$$

where $\mathbf{C}^T\mathbf{C} = 2\mathbf{I} + \mathbf{A}$. If the term $\gamma\mathbf{A}$ is ignored, we have

$$\hat{\mathbf{m}} = \left[\sum_{k=1}^{K}\frac{\mathbf{U}_k^T\mathbf{D}_1^{obs}}{\delta_k + 2\gamma/\delta_k}\mathbf{V}_k, \sum_{k=1}^{K}\frac{\mathbf{U}_k^T\mathbf{D}_2^{obs}}{\delta_k + 2\gamma/\delta_k}\mathbf{V}_k, \ldots, \sum_{k=1}^{K}\frac{\mathbf{U}_k^T\mathbf{D}_N^{obs}}{\delta_k + 2\gamma/\delta_k}\mathbf{V}_k\right]^T. \tag{10}$$
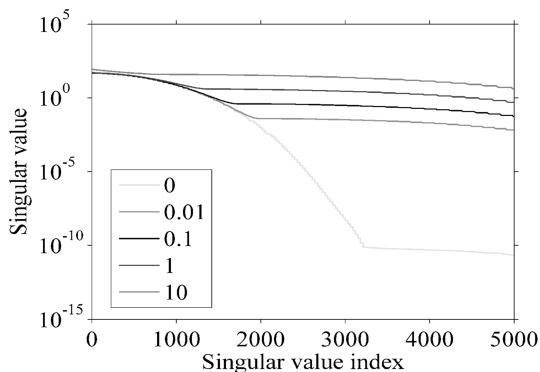
It is obvious that $\delta_k + 2\gamma/\delta_k \geq 2\sqrt{2\gamma}$, thus $\frac{\mathbf{U}_k^T\mathbf{D}_j^{obs}}{\delta_k + 2\gamma/\delta_k}$ will not be so large even for small δ_k if γ is not too small. In other words, the term $2\gamma/\delta_k$ plays a key role in reducing the amplification of noise. It demonstrates that the term $\gamma\mathbf{C}^T\mathbf{C}$ only derived from the regularization term includes a stabilization factor. If the term $\gamma\mathbf{A}$ is taken into account, the computation of the inverse of matrix $\mathbf{G}^T\mathbf{G} + \gamma\mathbf{C}^T\mathbf{C}$ is usually stable so long as γ is not too small, as denoted in Fig. 1 and also demonstrated by the synthetic and field examples in the following Examples section.

If we take the derivatives of $O_3(\hat{\mathbf{m}})$ with respect to variable $\mathbf{R}_{i,j}$, we have

$$\begin{aligned}
\frac{\partial O_3(\hat{\mathbf{m}})}{\partial \mathbf{R}_{i,j}} &= \mathbf{W}_i^T\left(\mathbf{WR}_j - \mathbf{D}_j^{obs}\right) + \gamma\left(2\mathbf{R}_{i,j}^{obs} - \mathbf{R}_{i,j-1}^{obs} - \mathbf{R}_{i,j+1}^{obs}\right) \\
&= \mathbf{W}_i^T\left(\mathbf{WR}_j - \mathbf{D}_j^{obs}\right) + \gamma[-1, 2, -1]\left[\mathbf{R}_{i,j-1}^{obs}, \mathbf{R}_{i,j}^{obs}, \mathbf{R}_{i,j+1}^{obs}\right]^T,
\end{aligned} \tag{11}$$

where vector $\mathbf{W}_i$ represents the i-th column of matrix $\mathbf{W}$, $\mathbf{R}_{i,j-1}^{obs}$, $\mathbf{R}_{i,j}^{obs}$ and $\mathbf{R}_{i,j+1}^{obs}$ represent the i-th elements at $(j-1)$-th column, j-th column and $(j+1)$-th column of matrix $\mathbf{R}$ respectively. Matrix $\mathbf{W}$ plays a temporal band-pass filtering role, eliminating the high- and low-frequency components of the reflectivity series $\mathbf{R}_j$ outside the frequency band of the wavelet. In other words, the data misfit term is not sensitivity to high- and low-frequency components of reflectivity. Vector $[-1, 2, -1]$ plays a spatial band-pass filtering role, which can mainly filter out the high-wavenumber components of the reflectivity series. Further, it can help overcoming lateral instability of the estimated reflectivity,

Fig. 1 Singular values of matrix $\mathbf{G}^T\mathbf{G} + \gamma\mathbf{C}^T\mathbf{C}$ with different parameters γ. Matrix $\mathbf{G}$ is constructed by a 30-Hz Ricker wavelet. When $\gamma = 0$, many singular values of matrix $\mathbf{G}^T\mathbf{G} + \gamma\mathbf{C}^T\mathbf{C}$ are very small and close to zero

probably mainly caused by the influence of high-wavenumber noise and/or the inconsistency of the energy and waveforms among seismic traces. Although a conventional spatial filter such as a smoothing filter can also be applied on the conventional deconvolution result to reduce the influence of the high-wavenumber noise, its operation works independently from the deconvolution. The smoothing filter can attenuate high-wavenumber noise, but meanwhile, they will deteriorate or destroy the match between the calculated data and the observed data. The spatial regularized deconvolution method, as an inversion technique, can simultaneously suppress high-wavenumber noise and keep the consistence with the data.

For the post-stack data, some seismic traces are sometimes missing, and/or some traces are probably relative poor-quality, such as low signal-to-noise ratio and arc phenomenon at the position of missing traces or faults caused by conventional migration. Generally, the robust inversion (e.g. Crase et al. 1990; Yuan et al. 2015) is a choice to deal with the undersampled data set or low quality migration data set to obtain an acceptable inversion result. In this paper, we illustrate that the spatial regularization can help recovering the reflectivity of the missing and/or poor-quality traces by slightly rewriting Eq. (8) as

$$O_4(\hat{\mathbf{m}}) = ||\mathbf{P}(\mathbf{d}^{obs} - \mathbf{G}\mathbf{m})||_2^2 + \gamma||\mathbf{C}\mathbf{m}||_2^2, \tag{12}$$

where matrix $\mathbf{P}$ is a restriction operator discarding missing and/or poor-quality traces. Note that the row of matrix $\mathbf{P}$ is not larger than its column, thereby essentially playing a dimensionality-reduction role for the data misfit term. However, $\mathbf{P}$ leads to an underdetermined linear equation. It is obvious that the reflectivity corresponding to the discarding traces cannot be recovered if there is no spatial constraint. In fact, Eq. (8) is a special case of Eq. (12), when $\mathbf{P} = \mathbf{I}$. To solve Eq. (12) can be broken up into two parts: live traces part and discarding traces part. For live traces case, the derivatives of $O_4(\hat{\mathbf{m}})$ with respect to variable $\mathbf{R}_{i,j}$ are in the same form as Eq. (11). For discarding traces case,

$$\frac{\partial O_4(\hat{\mathbf{m}})}{\partial \mathbf{R}_{i,j}} = \gamma\Big(2\mathbf{R}_{i,j}^{obs} - \mathbf{R}_{i,j-1}^{obs} - \mathbf{R}_{i,j+1}^{obs}\Big). \tag{13}$$

Let $\frac{\partial O_4(\hat{\mathbf{m}})}{\partial \mathbf{R}_{i,j}} = 0$, we get

$$\mathbf{R}_{i,j}^{obs} = \Big(\mathbf{R}_{i,j-1}^{obs} + \mathbf{R}_{i,j+1}^{obs}\Big)/2. \tag{14}$$

$\mathbf{R}_j^{obs}$ could be estimated by averaging its two neighboring estimated reflectivity traces. By repeatedly updating the reflectivity of the living traces and discarding traces, the frequency components of the reflectivity for the whole section or volume including discarding traces can be recovered. In essence, Eq. (14) reveals that the spatial regularization indeed can help exploring spatial continuities of the inverted model.

3 Examples

In this section, a 2D synthetic data example and a 2D field data example are used to illustrate the effectiveness of the spatial regularization in seismic deconvolution. We also compare spatial regularized deconvolution with conventional temporal deconvolution implemented by minimizing a data misfit and a L2 norm or a L1 norm of reflectivity to reveal the benefits of spatial regularized deconvolution.

We adopt different regularization schemes in the two examples, but use the same conjugate gradient (CG) algorithm (Trefethen and Bau 1997; Yuan and Wang 2013b) to iteratively solve the objective functions. Moreover, all deconvolution methods utilize all traces with the same initial model **0** and the maximum iteration number 30 to simultaneously invert for the whole reflectivity section.

3.1 Synthetic data example

A noisy synthetic data (Fig. 2a) is generated by adding 20 % random noise (the ratio of noise energy to signal energy is 20 %) to the convolution of a 30-Hz Ricker wavelet with

Fig. 2 The comparisons among the synthetic noisy data (**a**), the reference reflectivity (**b**) and the estimated reflectivity obtained by using different deconvolution methods: the spatial regularized deconvolution with the optimum regularization parameter 30 (**c**), the conventional deconvolution by using a L2 norm of model parameters as a regularization with the optimum regularization parameter 1.5 (**d**), the conventional deconvolution by using a L1 norm of model parameters as a regularization with the optimum regularization parameter 0.1 (**e**), and the unregularized deconvolution (**f**)

the reflectivity derived from a synthetic BG impedance model. The data set contains 700 traces with a sample interval of 2 ms. We use a 0-0-65-80 Hz band-pass filtered result of the original BG reflectivity as a reference (Fig. 2b), in order to concentrate on discussing the roles of the spatial regularization in seismic deconvolution. Compared with the reference reflectivity, the resolution of the original data (Fig. 2a) is lower and the stratigraphic contact relationship is harder to discontinuity than the reference reflectivity due to the wavelet interference and noise, denoted by the rectangles and ellipses in Fig. 2a and b.

We quantitatively define a relative error $E = ||\hat{\mathbf{m}} - \mathbf{m}_{ref}||_2^2 / ||\mathbf{m}_{ref}||_2^2$, where column vector $\mathbf{m}_{ref}$ represents the reference reflectivity, as an evaluation criterion to choose the optimum regularization parameter and appraise different deconvolution methods. The black curve with circles in Fig. 3 is the relative error E versus regularization parameter γ (called E-γ curve for short) of spatial regularized deconvolution. When $\gamma = 30$, the optimum deconvolution result can be obtained, as Fig. 2c shows. The blue curve with triangles in Fig. 3 is E-γ curve for using temporal regularized deconvolution implemented by minimizing a L2 norm of model parameters. It is obvious that when $\gamma = 1.5$, the optimum deconvolution result, as shown in Fig. 2d, is obtained. The red curve with asterisks in Fig. 3 is E-γ curve for using temporal regularized deconvolution implemented by minimizing a L1 norm of model parameters. When $\gamma = 0.1$, the optimum deconvolution result, as shown in Fig. 2e, is obtained. The two optimum regularization parameters for using temporal regularized deconvolution are also consistent to these obtained by using the classical L-curve method (Hansen 1992). For the sake of completeness, we also show the unregularized deconvolution result by setting $\gamma = 0$, shown in Fig. 2f. Figure 4 is the amplitude spectra of the original data (Fig. 2a), the reference (Fig. 2b) and deconvolution results obtained by using different methods (Fig. 2c–f). As both Fig. 2 in the time–space domain and Fig. 4 in the frequency-space domain show, the spatial regularization can help to stably invert for reflectivity (Fig. 2c, f), just like the regularization along the time direction (Fig. 2d, e). In addition, the spatial regularized deconvolution effectively reduces
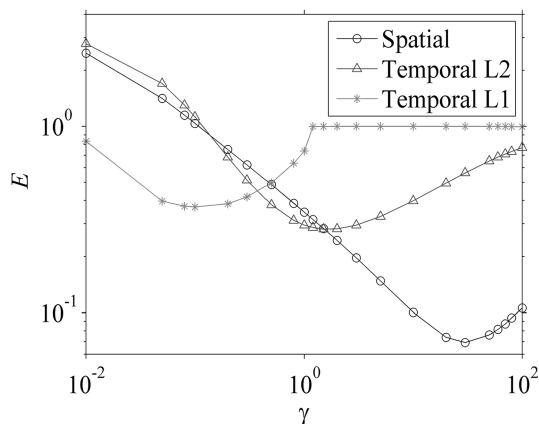

Fig. 3 The relative error E curves versus regularization parameter γ for using three different regularization methods: the spatial regularized deconvolution marked "Spatial" in the legend, the temporal regularized deconvolution adopting a L2 norm of model parameters as the regularization marked "Temporal L2" in the legend and the temporal regularized deconvolution adopting a L1 norm of model parameters as the regularization marked "Temporal L1" in the legend. The corresponding minimum relative errors of these three curves are 0.0693, 0.2804 and 0.3696, respectively
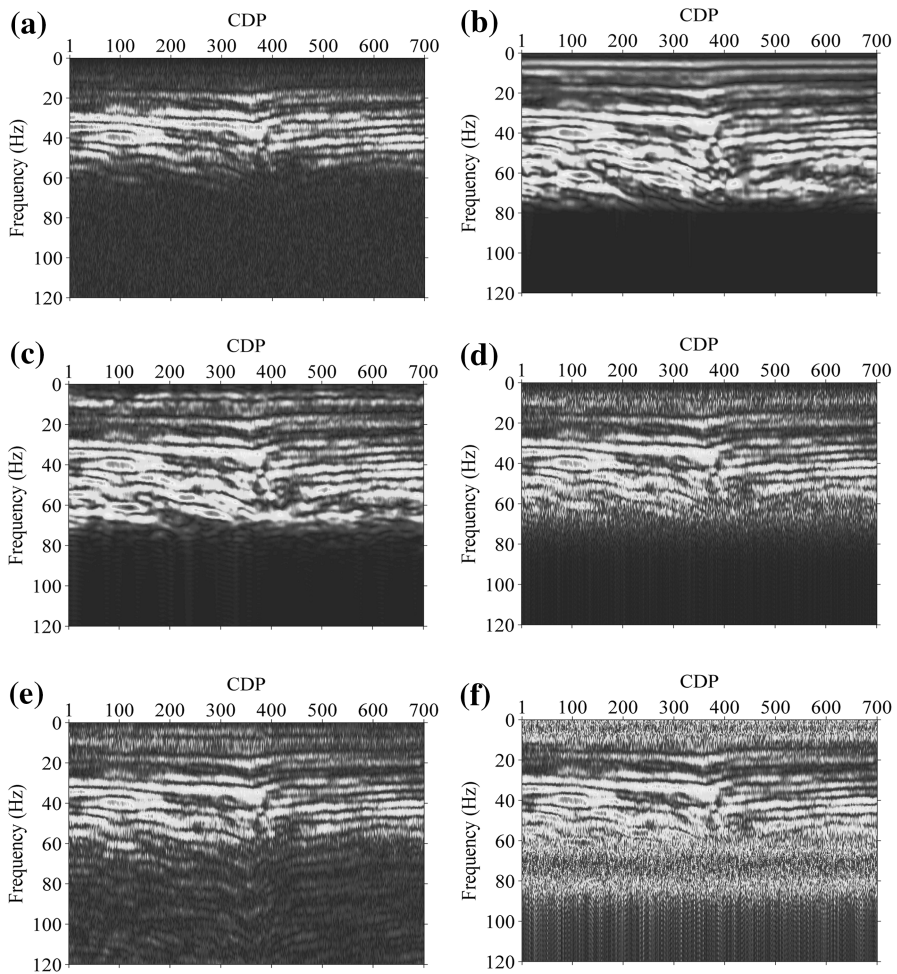
Fig. 4 The amplitude spectra corresponding to Fig. 2a–f

the influence of wavelet interference as denoted by the rectangles and ellipses in Fig. 2a–c, and gives rise to a high resolution and meanwhile high signal-to-noise ratio (SNR) result, which matches best with the reference. As well, the spatial regularized deconvolution avoids lateral instability of the inverted reflectivity, thereby preventing noisy trails like noodles always caused by the conventional temporal regularized deconvolution (Figs. 2d–e, 4d–e). It can be observed from Fig. 3 that the minimum relative errors of the two E-γ curves for using temporal regularized deconvolution are larger than that for using the spatial regularization. Figure 5 is the normalization wavenumber spectra of Fig. 2a–f, respectively. As Fig. 5 shows, the wavenumber components of spatial regularized deconvolution result is closest to those of the reference, whereas the wavenumber components of temporal regularized deconvolution result are still close to those of the original data.

In order to further illustrate the ability of the spatial regularization for evidently exploring the spatial continuities among traces, we randomly set 175 traces to be null, and a
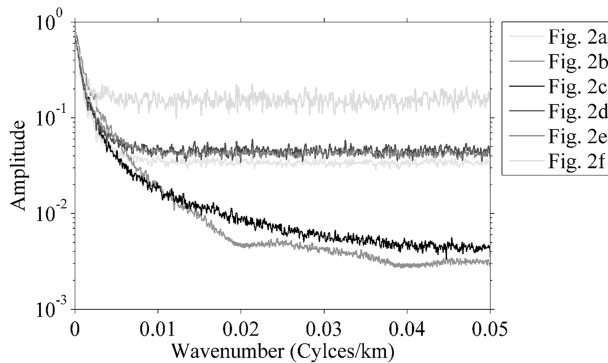
Fig. 5 The normalization wavenumber spectra corresponding to Fig. 2a–f. Every wavenumber spectrum curve is obtained by summing wavenumber spectra of all time slices and then normalizing

new synthetic section with 25 % discarding traces (Fig. 6a) is generated. By searching the smallest E value in the E-γ curve, we get the optimum deconvolution result, shown in Fig. 6b, when $\gamma = 20$. It can be observed form Fig. 6b that the spatial regularized deconvolution result for the data set is comparable to that for the full-sampled data set (Fig. 2c), even for the discarding traces. However, the conventional temporal regularized deconvolution methods cannot recover the reflectivity series corresponding to the discarding traces (not shown).

3.2 Field data example

A field post-stack seismic data is exploited to test the effectiveness of the spatial regularization for dealing with the real data. The dataset includes 608 traces with a sampling interval 1 ms, as shown in Fig. 7a. The deconvolution without regularization (Fig. 7e) yields a blurry result mainly aroused by the high-frequency model error above $\sim$80 Hz. When the smoothness or sparseness regularization of model parameters along the temporal direction is adopted, deconvolution result with the optimum regularization parameter obtained by using the classical L-curve method becomes stable, but includes some noisy trails like noodles and suffers from weak lateral instability (Fig. 7c, d). As expected,
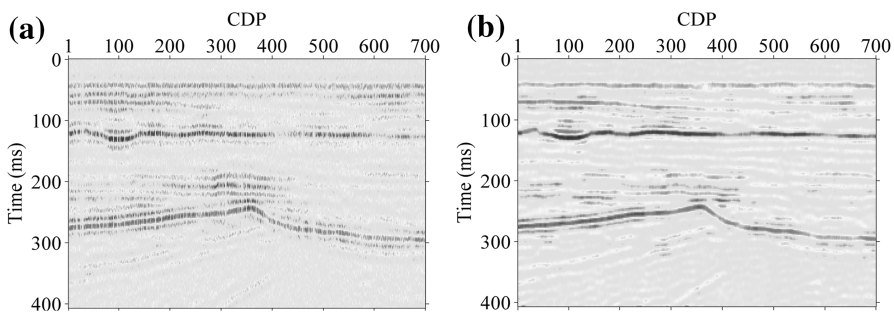

Fig. 6 The synthetic noisy data with 175 discarding traces (**a**) and the spatial regularized deconvolution result with the optimum regularization parameter 20 (**b**)
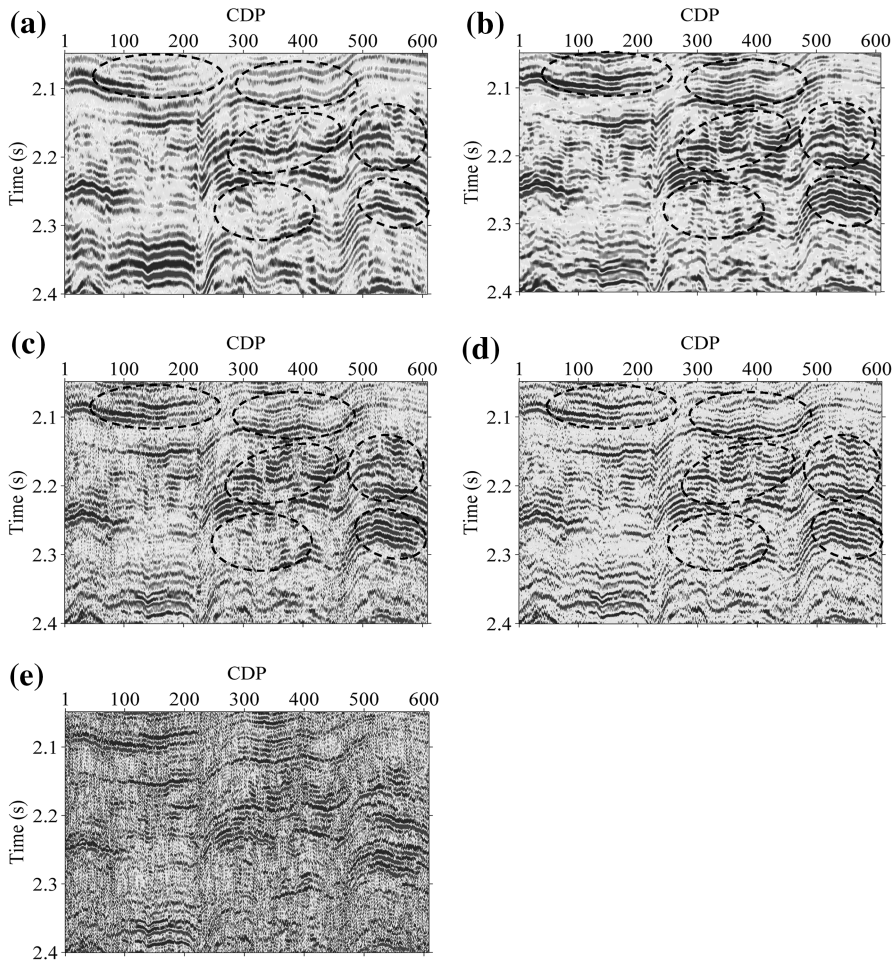
Fig. 7 The comparisons among the field seismic data (**a**) and the estimated reflectivity obtained by using different deconvolution methods: the spatial regularized deconvolution with the regularization parameter 10 (**b**), the conventional deconvolution by using a L2 norm of model parameters as a regularization with the optimum regularization parameter 0.5 (**c**), the conventional deconvolution by using a L1 norm of model parameters as a regularization with the optimum regularization parameter 0.1 (**d**), and the unregularized deconvolution (**e**). The regularization parameters for Fig. 6c and d are chosen by the classical L-curve method, whereas the regularization parameter for Fig. 6b is chosen by trial and error

the seismic deconvolution via the spatial regularization addresses these issues and yields a high resolution result with more clear details, as pointed out by the ellipses in Fig. 7b. These details improved by reducing wavelet interference also appear in temporal regularized deconvolution results (Fig. 7c, d). It is noticeable that the temporal regularized deconvolution methods do not introduce any constraints about spatial information of signals. The spatial regularized deconvolution does not visibly destroy the feature of structures thanks to the good trade-off between the data misfit term and the regularization term.

In order to clearly illustrate the continuity-preserving role of the spatial regularization, we also randomly set 152 traces to be null and generate a new section (Fig. 8a). Therefore,
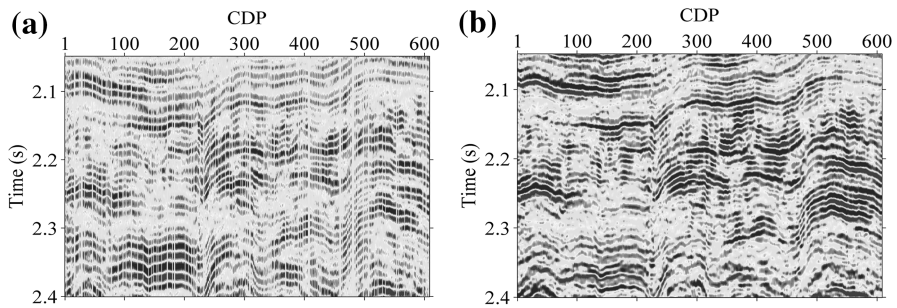
(a)

(b)

Fig. 8 The field data with 152 discarding traces (**a**) and the spatial regularized deconvolution result (**b**) with the optimum regularization parameter 5 which is chosen by trial and error

only 456 traces are utilized to implement 608 traces deconvolution. The result is shown in Fig. 8b. By comparing Fig. 8b with Fig. 7b, we find that the spatial regularized deconvolution result considering some discarded traces out of the inversion is close to that for processing the whole data. The recovery of the reflectivity for the discarded traces demonstrates that the spatial regularization indeed help exploiting the spatial (local) continuities among traces.

4 Conclusions

The spatial regularization used in seismic deconvolution plays important roles in preventing the lateral instability of the estimated reflectivity, exploring spatial continuities among traces, and stabilizing reflectivity inversion. Compared with the conventional deconvolution adopting temporal regularization implemented by a L2 norm or a L1 norm of model parameters, spatial regularized deconvolution yields the higher resolution and meanwhile high SNR deconvolution result, mainly attributed to the optimal trade-off between the multi-trace data misfit term and the spatial regularization term. Different from the temporal regularization via a L1 norm, the spatial regularization has a limitation that it cannot help recovering information outside frequency band of seismic signal. Although we only show 2D data examples in this paper, our objective function Eq. (12) can be directly adopted to simultaneously process 3D seismic data.

References

Baziw E, Ulrych TJ (2006) Principle phase decomposition: a new concept in blind seismic deconvolution. IEEE Trans Geosci Remote Sens 44:2271–2281
Crase E, Pica A, Noble M, McDonald J, Tarantola A (1990) Robust elastic nonlinear waveform inversion: application to real data. Geophysics 55:527–538
Debeye HWJ, van Riel P (1990) Lp-norm deconvolution. Geophys Prospect 38:381–403

Gholami A, Sacchi MD (2013) Fast 3D blind seismic deconvolution via constrained total variation and GCV. SIAM J Imagine Sci 6:2350–2369

Hansen PC (1992) Analysis of discrete ill-posed problems by means of the L-curve. SIAM Rev 34:561–580

Heimer A, Cohen I (2008) Multichannel blind seismic deconvolution using dynamic programming. Signal Process 88:1839–1851

Herrmann FJ (2005) Seismic deconvolution by atomic decomposition: a parametric approach with sparseness constraints. Integr Comput Aided Eng 12:69–90

Kaaresen KF, Taxt T (1998) Multichannel blind deconvolution of seismic signals. Geophysics 63:2093–2107

Kumar V (2009) Incoherent noise suppression and deconvolution using curvelet-domain sparsity. Master thesis, the University of British Columbia

Lavielle M (1991) 2-D Bayesian deconvolution. Geophysics 56:2008–2018

Levy S, Fullagar PK (1981) Reconstruction of a sparse spike train from a portion of its spectrum and application to high-resolution deconvolution. Geophysics 46:1235–1243

Robinson EA (1984) Seismic inversion and deconvolution. Classical methods. Geophysical Press, Part A

Robinson EA, Treitel S (1980) Geophysical signal analysis. Prentice-Hall Inc., New Jersey

Sacchi MD (1997) Reweighting strategies in seismic deconvolution. Geophys J Int 129:651–656

Taylor HL, Banks SC, McCoy JF (1979) Deconvolution with the l1-norm. Geophysics 49:39–52

Trefethen LN, Bau D (1997) Numerical linear algebra. Society for Industrial and Applied Mathematics (SIAM), Philadelphia

Wang JF, Wang XS, Perz M (2006) Structure-preserving regularization for sparse deconvolution. 76th Annual International Meeting, SEG, Expanded Abstracts, pp. 2072–2076

Wu HZ, Fu LY, Meng XH (2007) Blind deconvolution of seismic signals with non-white reflectivities. Explor Geophys 38:235–241

Yuan SY, Wang SX (2011) Influence of inaccurate wavelet phase estimation on seismic inversion estimation on seismic inversion. Appl Geophys 8:48–59

Yuan SY, Wang SX (2013a) Spectral sparse Bayesian learning reflectivity inversion. Geophys Prospect 61:735–746

Yuan SY, Wang SX (2013b) Edge-preserving noise reduction based on Bayesian inversion with directional difference constraints. J Geophys Eng 10:025001

Yuan SY, Wang SX, Li GF (2012) Random noise reduction using Bayesian inversion. J Geophys Eng 9:60–68

Yuan SY, Wang SX, Luo CM, He YX (2015) Simultaneous multitrace impedance inversion with transform-domain sparsity promotion. Geophysics 80:R71–R80

Zhang R, Sen MK, Srinivasan S (2013) Multi-trace basis pursuit inversion with spatial regularization. J Geophys Eng 10:035012